

# **Towards the high-throughput synthesis of bulk materials: thermoelectric PbTe-PbSe-SnTe-SnSe alloys**

Brenden R. Ortiz,\* Jesse M. Adamczyk, Kiarash Gordiz, Tara Braden, and Eric S. Toberer\*

*Colorado School of Mines, Golden, Colorado 80401, United States*

E-mail: bortiz@mines.edu; etoberer@mines.edu

## **Electronic Supplementary Information**

In this supplementary section, we provide additional data to augment the results provided within the main body of “Towards the high-throughput synthesis of bulk materials: thermoelectric PbTe-PbSe-SnTe-SnSe alloys.” Select traces along pseudobinary lines used to generate solubility limits *via* Vegard’s Law are shown. All heat maps used in the main body are included again alongside the raw data used to generate the plots. Additional heat maps not used in the main text (e.g. Hall mobility, effective mass) are also included.

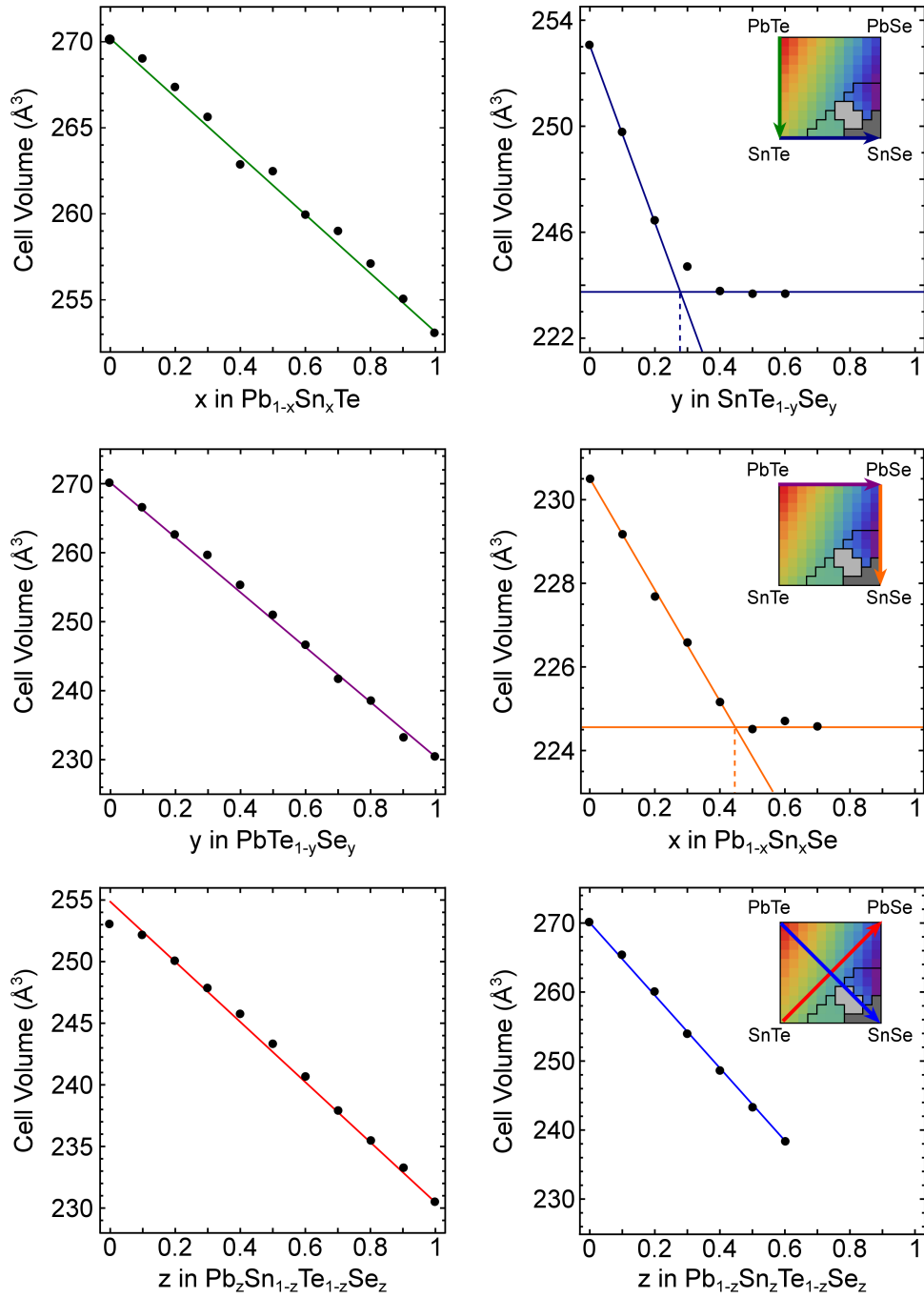
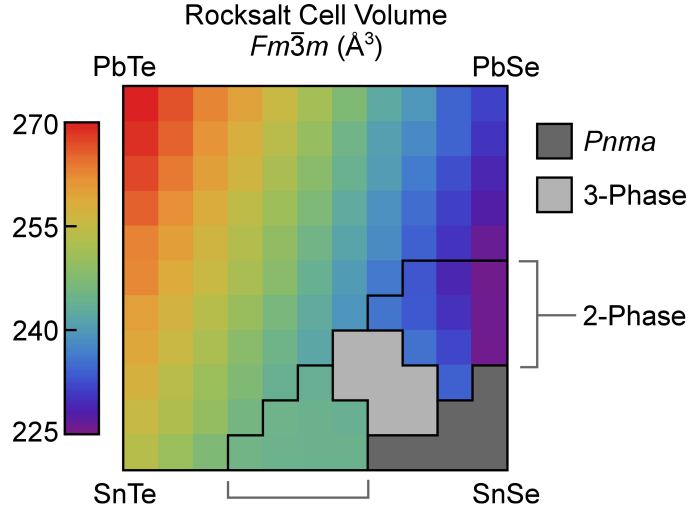
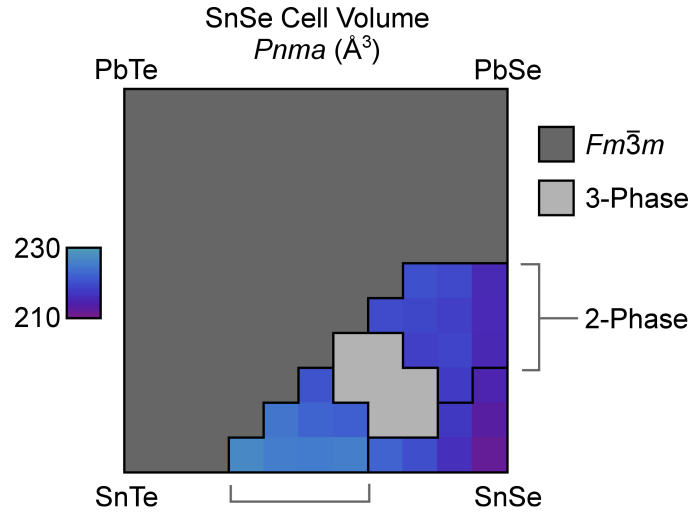


Figure S1: Select traces showing Vegard's Law and solubility determination along the pseudobinary edges and diagonals of the PbTe-PbSe-SnTe-SnSe alloying system. Consistent with literature, all combinations of rocksalt phases yield full solid solutions. For systems that show reduced solubility (e.g. rocksalt-SnSe combinations), solubility limits were determined by interpolation (dashed lines). For the PbTe-SnSe diagonal, we roughly estimate the solubility limit at 60% SnSe.



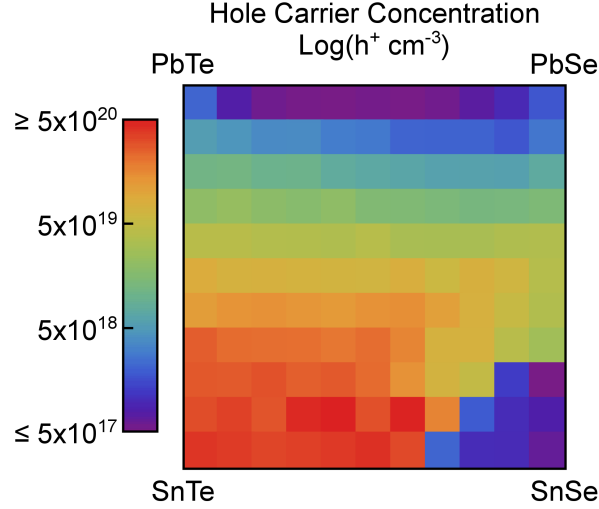
	%Se											
<b>PbTe</b>	0.0	0.1	0.2	0.3	0.4	0.5	0.6	0.7	0.8	0.9	1.0	<b>PbSe</b>
0.0	270.12	266.61	262.69	259.67	255.30	251.08	246.67	241.66	238.61	233.21	230.49	0.0
0.1	269.01	265.49	261.46	257.52	253.45	249.33	244.41	239.91	237.01	233.25	229.17	0.1
0.2	267.40	263.72	260.03	256.48	251.73	247.67	243.59	239.39	235.50	231.57	227.70	0.2
0.3	265.60	261.83	258.18	254.05	250.22	246.28	241.89	237.92	234.18	230.27	226.59	0.3
0.4	262.88	260.21	256.42	252.58	248.66	244.72	240.69	237.18	233.05	229.05	225.16	0.4
<b>%Sn</b> 0.5	262.51	258.54	255.22	251.62	247.67	243.29	239.27	235.11	232.12	227.73	224.52	0.5
0.6	259.95	256.91	253.15	249.66	245.73	242.04	238.37	234.83	232.36	228.83	224.69	0.6
0.7	259.02	255.37	251.88	247.81	244.33	241.17	x	x	234.54	230.81	224.58	0.7
0.8	257.10	253.45	250.05	246.56	243.27	242.97	x	x	x	233.03		0.8
0.9	255.04	252.23	249.04	245.08	244.16	243.62	243.19	x	x			0.9
1.0	253.08	249.81	246.44	244.70	243.81	243.67	243.69					1.0
<b>SnTe</b>	0.0	0.1	0.2	0.3	0.4	0.5	0.6	0.7	0.8	0.9	1.0	<b>SnSe</b>

Figure S2: Rocksalt ( $Fm\bar{3}m$ ) lattice parameter heat map with associated data. Data in table is in units of  $\text{\AA}^3$ . All rocksalt-based mixtures exhibit full solid solubility, consistent with literature. Pairwise combinations of rocksalt phases and SnSe always exhibit reduced solubility. Phase boundaries are outlined in black. The two-phase regions (rocksalt + SnSe) are indicated by the grey brackets. We also note a small region that exhibits three-phase mixtures, indicating the possibility of a miscibility gap in the rocksalt phases. Due to excessive peak overlap, three-phase regions were not refined, they are denoted by an ‘x’ in the table.



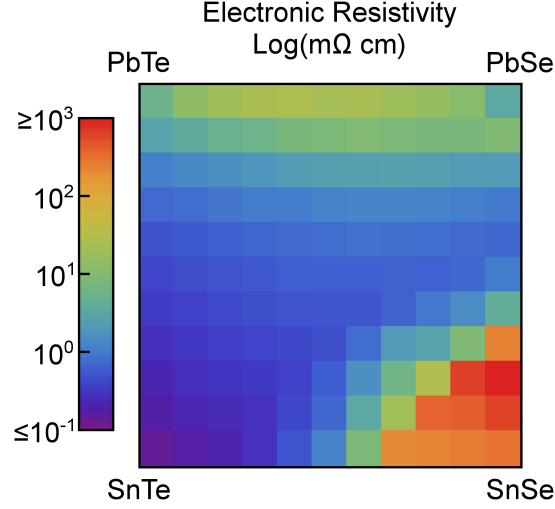
	%Se											
<b>PbTe</b>	0.0	0.1	0.2	0.3	0.4	0.5	0.6	0.7	0.8	0.9	1.0	<b>PbSe</b>
0.0												0.0
0.1												0.1
0.2												0.2
0.3												0.3
0.4												0.4
<b>%Sn</b> 0.5									219.91	219.16	215.39	0.5
0.6								219.41	218.95	218.10	215.32	0.6
0.7							x	x	218.13	218.63	215.26	0.7
0.8						220.29	x	x	x	217.51	214.58	0.8
0.9					224.13	222.22	221.43	x	x	217.23	212.95	0.9
1.0				226.70	225.10	225.03	225.32	222.09	219.85	216.03	211.83	1.0
<b>SnTe</b>	0.0	0.1	0.2	0.3	0.4	0.5	0.6	0.7	0.8	0.9	1.0	<b>SnSe</b>

Figure S3: SnSe ( $Pnma$ ) lattice parameter heat map with associated data. Data in table is in units of  $\text{\AA}^3$ . SnSe single phase region exhibits retrograde solubility, wherein the highest entropy direction (PbTe-SnSe pseudobinary) actually exhibits the least solubility. Phase boundaries are outlined in black. The two-phase regions (rocksalt + SnSe) are indicated by the grey brackets. Due to excessive peak overlap, three-phase regions were not refined, they are denoted by an 'x' in the table.



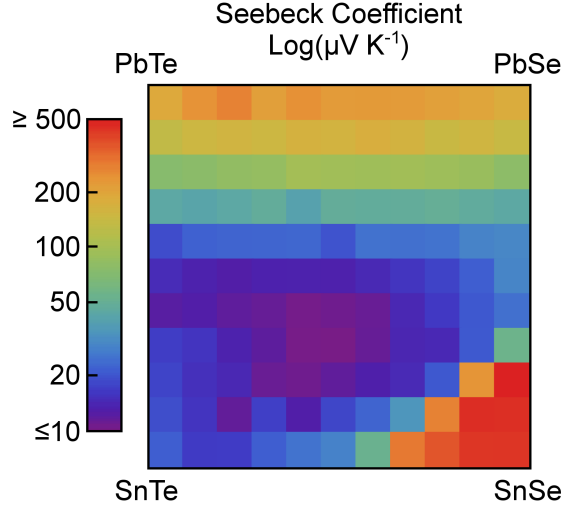
	% Se												
<b>PbTe</b>	0.0	0.1	0.2	0.3	0.4	0.5	0.6	0.7	0.8	0.9	1.0	<b>PbSe</b>	
0.0	2.07	0.75	0.55	0.51	0.45	0.53	0.50	0.54	0.69	0.91	1.69	0.0	
0.1	5.23	4.37	3.58	3.64	2.85	2.69	2.02	2.00	2.01	1.70	2.58	0.1	
0.2	11.18	11.65	9.80	10.00	7.55	6.81	6.38	5.70	5.79	5.63	7.26	0.2	
0.3	19.72	22.13	18.65	17.12	19.76	15.18	14.83	13.71	12.46	12.81	14.39	0.3	
0.4	40.91	40.58	36.92	36.31	34.54	39.96	30.98	30.76	31.00	34.57	35.55	0.4	
<b>%Sn</b>	0.5	86.69	73.54	74.78	71.53	67.72	65.55	80.25	57.91	77.00	64.17	38.36	0.5
	0.6	115.64	138.89	143.56	132.93	124.22	141.70	147.62	109.75	76.24	53.11	35.85	0.6
	0.7	267.31	229.90	223.60	220.80	201.09	226.32	167.81	72.85	74.00	40.47	27.03	0.7
	0.8	283.48	276.02	303.33	263.65	278.84	230.90	142.50	69.58	49.48	1.21	0.30	0.8
	0.9	317.77	359.71	295.67	463.10	512.49	305.80	493.85	171.36	1.79	0.96	0.77	0.9
	1.0	407.25	384.44	344.07	361.66	389.19	431.55	330.16	2.07	0.96	0.95	0.62	1.0
<b>SnTe</b>	0.0	0.1	0.2	0.3	0.4	0.5	0.6	0.7	0.8	0.9	1.0	<b>SnSe</b>	

Figure S4: Hall carrier concentration heat map with associated raw data. Data in table is in units of  $10^{18} \text{ h}^+ \text{ cm}^{-3}$ . Within the rocksalt single-phase region, we note that the carrier concentration depends strongly on the Sn content. As all rocksalt phases share full solid solution, we expect changes in the carrier concentration from the intrinsic (e.g. PbTe, PbSe) to degenerate (e.g. SnTe) samples. However, these statements are merely empirical, and we note that there is not a good *mechanistic* explanation for the trend in carrier concentration.



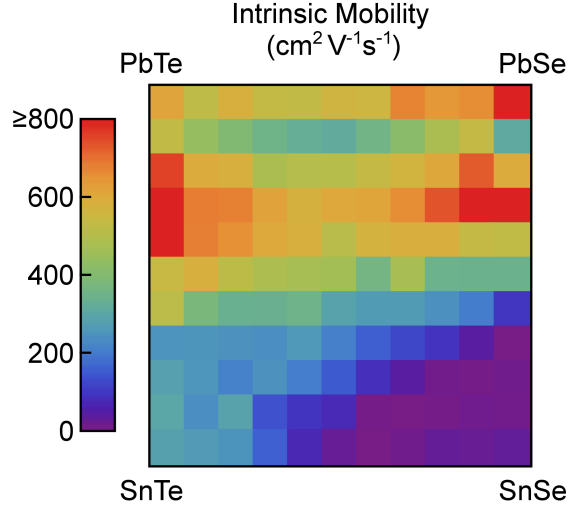
		%Se												
		0.0	0.1	0.2	0.3	0.4	0.5	0.6	0.7	0.8	0.9	1.0	PbSe	
%Sn	PbTe	0.0	5.40	13.68	20.10	24.67	27.29	22.44	23.79	18.25	15.27	11.30	3.36	0.0
	0.1	2.72	3.77	5.04	5.64	7.56	8.33	9.60	8.60	7.58	7.91	9.23	0.1	
	0.2	1.08	1.30	1.54	1.80	2.18	2.43	2.46	2.57	2.40	2.10	2.08	0.2	
	0.3	0.71	0.76	0.89	1.02	1.02	1.17	1.19	1.20	1.16	1.05	0.96	0.3	
	0.4	0.47	0.55	0.62	0.68	0.73	0.77	0.80	0.79	0.78	0.72	0.70	0.4	
	0.5	0.38	0.43	0.49	0.54	0.58	0.61	0.62	0.63	0.62	0.69	1.00	0.5	
	0.6	0.33	0.36	0.41	0.45	0.48	0.51	0.51	0.62	0.93	1.42	4.13	0.6	
	0.7	0.25	0.30	0.34	0.38	0.40	0.44	0.76	2.06	2.67	8.90	244.84	0.7	
	0.8	0.21	0.25	0.28	0.31	0.36	0.57	1.55	6.04	28.65	657.08	1458.12	0.8	
	0.9	0.17	0.20	0.23	0.26	0.39	0.70	3.26	21.12	397.72	430.61	639.35	0.9	
	1.0	0.13	0.17	0.20	0.26	0.50	1.17	8.52	210.23	232.24	269.08	319.44	1.0	
SnTe		0.0	0.1	0.2	0.3	0.4	0.5	0.6	0.7	0.8	0.9	1.0	SnSe	

Figure S5: Electronic resistivity heat map with associated raw data. Data in table is in units of  $m\Omega\text{ cm}$ . The resistivity shows smooth, continuous changes throughout the PbTe-PbSe-SnTe-SnSe alloying system, indicative of excellent sample quality. Trends are consistent with the basic material properties of the pure endpoints (lightly p-type PbTe and PbSe, degenerate p-type SnTe, and intrinsic SnSe).



		%Se												
		0.0	0.1	0.2	0.3	0.4	0.5	0.6	0.7	0.8	0.9	1.0	PbSe	
%Sn	PbTe	0.0	205.21	252.85	283.68	225.87	257.77	235.27	237.78	236.25	223.69	212.56	196.38	0.0
	0.1	145.79	162.84	172.51	163.68	180.23	175.68	189.24	176.96	157.50	169.83	155.22	0.1	
	0.2	85.92	88.87	94.63	97.34	111.59	108.62	106.75	109.48	106.04	100.85	90.63	0.2	
	0.3	53.37	50.60	53.38	57.98	49.01	58.37	57.43	57.62	59.87	56.53	53.55	0.3	
	0.4	24.54	28.00	28.60	28.85	29.36	25.63	31.64	31.14	31.90	35.96	37.41	0.4	
	0.5	19.47	17.98	17.16	17.88	17.95	17.84	19.05	20.90	23.05	27.52	36.64	0.5	
	0.6	16.62	17.20	15.96	15.36	14.22	14.64	15.26	18.84	21.54	26.43	31.12	0.6	
	0.7	22.19	20.83	17.92	16.12	14.04	13.94	15.43	18.61	18.95	26.65	65.67	0.7	
	0.8	23.20	20.15	18.87	15.16	14.64	15.88	17.55	19.18	26.45	248.82	488.58	0.8	
	0.9	24.84	20.83	15.71	22.56	17.29	23.52	28.62	42.46	284.84	458.38	452.98	0.9	
1.0	27.47	21.77	21.92	27.55	31.85	35.73	63.33	303.21	370.31	437.45	439.97	1.0		
SnTe		0.0	0.1	0.2	0.3	0.4	0.5	0.6	0.7	0.8	0.9	1.0	SnSe	

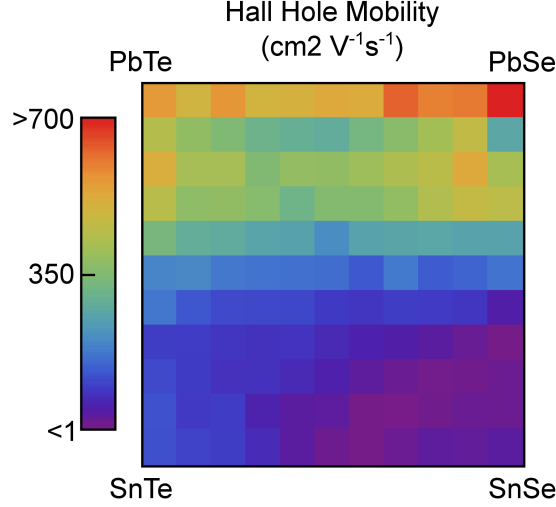
Figure S6: Seebeck coefficient heat map with associated raw data. Data in table is in units of  $\mu\text{V K}^{-1}$ . The Pb-rich compositions exhibit trends consistent with the trends observed in the Hall carrier concentration. However, there is a region of low Seebeck coefficient in the center of the map which does not coincide with the changes in the carrier concentration. We note that this phenomenon is consistent with the emergence of band-inversion, which has been previously noted around 60% SnTe along the PbTe-SnTe pseudobinary. We also observe a minimum in Seebeck at 60% SnTe, suggesting that the reduced Seebeck is indicative of band inversion.



		%Se										
<b>PbTe</b>	0.0	0.1	0.2	0.3	0.4	0.5	0.6	0.7	0.8	0.9	1.0	<b>PbSe</b>
0.0	616.50	524.08	586.37	535.90	532.11	567.62	558.68	676.73	643.78	661.31	1224.12	0.0
0.1	531.85	441.94	397.77	356.06	330.15	319.94	362.08	415.61	484.99	537.69	312.00	0.1
0.2	760.61	599.81	585.51	484.82	504.44	507.71	538.00	570.70	609.29	730.31	596.85	0.2
0.3	802.79	686.82	681.12	620.75	577.30	608.76	615.42	661.49	740.00	818.35	812.22	0.3
0.4	845.53	684.27	656.73	606.27	584.67	514.25	575.34	589.31	589.19	537.15	529.17	0.4
<b>%Sn</b> 0.5	544.83	587.21	522.03	488.49	477.16	470.67	366.67	479.05	347.56	344.09	346.07	0.5
0.6	518.12	382.85	341.17	341.38	352.83	288.00	268.52	268.38	242.89	205.47	97.10	0.6
0.7	250.25	253.76	247.83	238.47	262.70	212.01	159.26	124.39	92.42	43.01	3.06	0.7
0.8	282.46	255.00	215.05	247.58	206.85	151.21	85.60	43.19	12.87	8.88	13.50	0.8
0.9	300.42	238.09	289.66	138.09	94.71	77.20	9.30	3.45	9.10	15.26	12.79	0.9
1.0	283.64	267.70	250.82	159.69	73.05	26.72	3.71	14.83	28.50	24.71	31.74	1.0
<b>SnTe</b>	0.0	0.1	0.2	0.3	0.4	0.5	0.6	0.7	0.8	0.9	1.0	<b>SnSe</b>

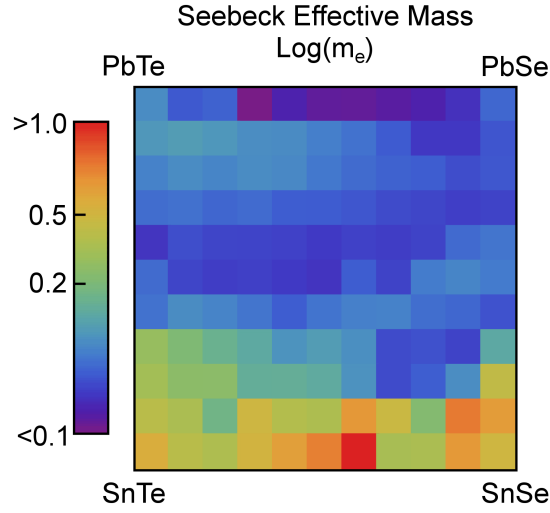
Figure S7: Intrinsic mobility heat map with associated raw data. Data in table is in units of  $\text{cm}^2 \text{V}^{-1} \text{s}^{-1}$ . The intrinsic mobility corrects for changes in the carrier concentration, allowing us to resolve the underlying intrinsic transport. We note several regions of increased mobility, which may allow for improved thermoelectric performance within the alloy. As the correction to intrinsic mobility is based on the single parabolic band model, it will not provide particularly good estimations in SnSe (resistive, possible bipolar contributions) or pure SnTe (metallic with exceptionally low Seebeck).





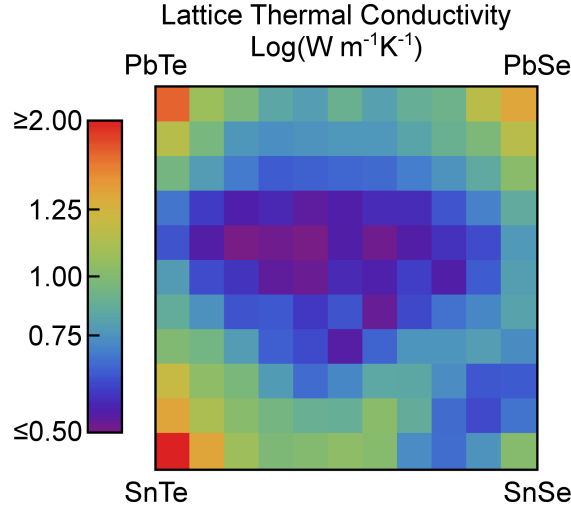
	%Se											
<b>PbTe</b>	0.0	0.1	0.2	0.3	0.4	0.5	0.6	0.7	0.8	0.9	1.0	<b>PbSe</b>
0.0	558.93	495.13	563.45	495.98	504.28	529.51	522.19	631.78	594.66	604.31	1098.34	0.0
0.1	438.49	377.00	345.00	304.20	289.80	278.90	321.90	363.02	409.62	464.30	262.35	0.1
0.2	516.30	412.70	413.00	345.77	378.96	377.60	397.52	425.70	449.06	528.05	413.88	0.2
0.3	445.63	372.39	378.12	357.28	308.60	351.40	352.75	379.70	431.87	465.85	451.53	0.3
0.4	327.65	282.46	273.84	253.85	246.85	203.48	251.65	255.83	258.70	249.43	250.26	0.4
<b>%Sn</b> 0.5	188.70	195.61	169.96	162.28	158.82	156.19	125.65	171.75	130.67	140.87	162.10	0.5
0.6	166.06	124.79	107.19	105.25	104.72	86.71	82.52	91.47	88.37	82.51	42.14	0.6
0.7	92.37	90.83	82.42	75.29	77.48	62.31	49.21	42.14	31.59	17.34	1.86	0.7
0.8	106.53	89.81	73.35	75.84	62.28	47.39	28.18	14.85	5.17	8.37	13.45	0.8
0.9	117.10	85.22	90.30	51.38	30.95	29.31	3.88	1.73	8.75	15.18	12.72	0.9
1.0	116.02	97.90	92.03	65.41	32.05	12.37	2.22	14.37	28.08	24.54	31.53	1.0
<b>SnTe</b>	0.0	0.1	0.2	0.3	0.4	0.5	0.6	0.7	0.8	0.9	1.0	<b>SnSe</b>

Figure S8: Experimental Hall mobility heat map with associated raw data. Data in table is in units of  $\text{cm}^2 \text{V}^{-1} \text{s}^{-1}$ . Unlike the intrinsic mobility map, the raw Hall mobility data depends dramatically on the carrier concentration. However, despite the strong dependence on the carrier concentration, we can still resolve some regions of improved mobility within the alloy. Again, the performance of SnSe is likely underestimated due to the incredibly low carrier densities.



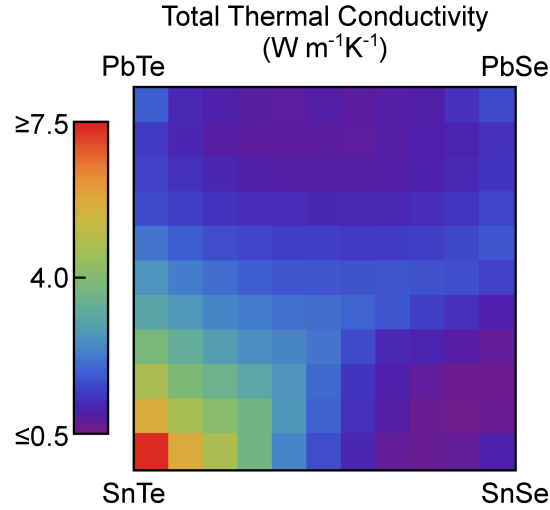
		%Se												
		0.0	0.1	0.2	0.3	0.4	0.5	0.6	0.7	0.8	0.9	1.0	PbSe	
%Sn	PbTe	0.0	0.23	0.18	0.18	0.11	0.13	0.12	0.12	0.12	0.13	0.14	0.19	0.0
	0.1	0.25	0.26	0.25	0.24	0.23	0.21	0.20	0.18	0.15	0.15	0.17	0.1	
	0.2	0.22	0.23	0.22	0.23	0.23	0.21	0.19	0.18	0.18	0.17	0.17	0.2	
	0.3	0.19	0.20	0.19	0.19	0.18	0.18	0.17	0.17	0.16	0.15	0.16	0.3	
	0.4	0.15	0.17	0.16	0.16	0.16	0.15	0.16	0.15	0.16	0.19	0.20	0.4	
	0.5	0.19	0.16	0.15	0.16	0.15	0.15	0.18	0.16	0.21	0.22	0.21	0.5	
	0.6	0.20	0.23	0.22	0.20	0.18	0.20	0.22	0.22	0.20	0.19	0.17	0.6	
	0.7	0.47	0.40	0.34	0.30	0.24	0.26	0.24	0.16	0.17	0.16	0.30	0.7	
	0.8	0.51	0.43	0.43	0.32	0.32	0.30	0.24	0.16	0.18	0.24	0.62	0.8	
	0.9	0.59	0.53	0.35	0.68	0.56	0.54	0.90	0.66	0.41	1.06	0.88	0.9	
1.0	0.76	0.58	0.55	0.71	0.86	1.03	1.52	0.52	0.53	0.89	0.69	1.0		
SnTe	SnSe	0.0	0.1	0.2	0.3	0.4	0.5	0.6	0.7	0.8	0.9	1.0	SnSe	

Figure S9: Density of states effective mass heat map with associated raw data. Data in table is in units of the electron mass ( $m_e$ ). The effective mass shows very little variation over much of the alloying space. However, we do note a transition to higher effective masses after the band convergence at 60% SnTe along the PbTe-SnTe pseudobinary edge. We are cautious when interpreting the effective mass data, as they are generated from single point Seebeck Pisarenko fits.



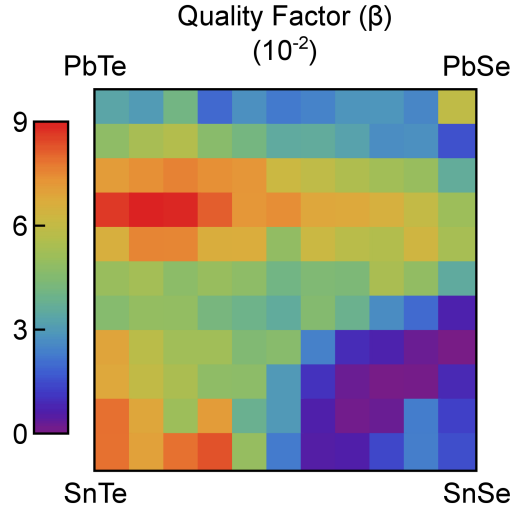
		%Se												
		0.0	0.1	0.2	0.3	0.4	0.5	0.6	0.7	0.8	0.9	1.0	PbSe	
%Sn	PbTe	0.0	1.73	1.08	0.95	0.82	0.78	0.88	0.79	0.86	0.89	1.20	1.43	0.0
	0.1	1.19	0.94	0.75	0.73	0.74	0.75	0.76	0.81	0.87	0.95	1.19	0.1	
	0.2	0.92	0.77	0.68	0.63	0.64	0.64	0.65	0.69	0.74	0.83	1.00	0.2	
	0.3	0.67	0.58	0.53	0.54	0.51	0.52	0.55	0.55	0.61	0.70	0.84	0.3	
	0.4	0.61	0.52	0.47	0.49	0.46	0.52	0.49	0.52	0.56	0.60	0.76	0.4	
	0.5	0.77	0.60	0.56	0.51	0.50	0.55	0.53	0.58	0.52	0.63	0.78	0.5	
	0.6	0.85	0.74	0.61	0.62	0.57	0.61	0.50	0.60	0.67	0.71	0.80	0.6	
	0.7	0.97	0.92	0.77	0.63	0.60	0.52	0.64	0.75	0.75	0.78	0.73	0.7	
	0.8	1.26	1.02	0.94	0.77	0.65	0.71	0.82	0.82	0.73	0.62	0.62	0.8	
	0.9	1.43	1.14	1.00	0.92	0.87	0.86	1.00	0.85	0.66	0.60	0.67	0.9	
1.0	2.02	1.43	1.08	0.96	0.98	1.02	0.99	0.72	0.66	0.74	0.99	1.0		
SnTe		0.0	0.1	0.2	0.3	0.4	0.5	0.6	0.7	0.8	0.9	1.0	SnSe	

Figure S10: Lattice thermal conductivity heat map with associated raw data. Data in table is in units of  $\text{W m}^{-1}\text{K}^{-1}$ . The lattice thermal conductivity shows the carrier concentration independent heat conduction, allowing us to examine the effect of alloying on the lattice independent from changes in the electronic transport. The lattice thermal conductivity trends intuitively – with reduced values occurring in the heavily alloyed samples (i.e. increased point-defect scattering). We note that the lattice thermal conductivity shows a minima which is offset from the central composition.



		%Se												
		0.0	0.1	0.2	0.3	0.4	0.5	0.6	0.7	0.8	0.9	1.0	PbSe	
%Sn	PbTe	0.0	1.82	1.11	0.97	0.84	0.79	0.90	0.81	0.89	0.92	1.24	1.57	0.0
	0.1	1.38	1.07	0.85	0.82	0.81	0.81	0.81	0.86	0.94	1.02	1.24	0.1	
	0.2	1.47	1.23	1.06	0.95	0.89	0.88	0.88	0.91	0.98	1.10	1.28	0.2	
	0.3	1.60	1.45	1.27	1.18	1.16	1.08	1.09	1.09	1.17	1.32	1.52	0.3	
	0.4	2.15	1.82	1.62	1.54	1.43	1.45	1.37	1.41	1.46	1.56	1.75	0.4	
	0.5	2.66	2.27	2.04	1.85	1.74	1.73	1.70	1.73	1.68	1.65	1.48	0.5	
	0.6	3.08	2.75	2.40	2.25	2.08	2.04	1.92	1.75	1.44	1.21	0.97	0.6	
	0.7	3.81	3.33	2.91	2.56	2.41	2.16	1.60	1.10	1.02	0.86	0.73	0.7	
	0.8	4.72	3.88	3.51	3.10	2.67	1.98	1.29	0.94	0.75	0.62	0.62	0.8	
	0.9	5.68	4.67	4.10	3.65	2.71	1.89	1.22	0.88	0.66	0.60	0.67	0.9	
1.0	7.40	5.76	4.72	3.65	2.38	1.62	1.07	0.73	0.66	0.75	0.99	1.0		
SnTe		0.0	0.1	0.2	0.3	0.4	0.5	0.6	0.7	0.8	0.9	1.0	SnSe	

Figure S11: Total thermal conductivity heat map with associated raw data. Data in table is in units of  $\text{W m}^{-1}\text{K}^{-1}$ . The total thermal conductivity convolutes both the electronic and lattice components of heat transport. As such, the overall trend is roughly a convolution of the lattice thermal conductivity and the resistivity heat maps.



		%Se											
		0.0	0.1	0.2	0.3	0.4	0.5	0.6	0.7	0.8	0.9	1.0	PbSe
%Sn	PbTe	3.38	3.06	4.14	2.00	2.76	2.29	2.47	2.89	2.89	2.55	5.94	0.0
	0.1	4.83	5.40	5.65	4.70	4.20	3.56	3.62	3.27	2.71	2.76	1.59	0.1
	0.2	7.16	7.40	7.65	7.40	7.29	6.22	5.92	5.55	5.27	5.03	3.66	0.2
	0.3	8.67	9.00	8.92	8.18	7.27	7.44	6.86	6.82	6.58	6.03	5.16	0.3
	0.4	6.61	7.59	7.58	6.67	6.69	4.91	6.20	5.79	5.63	6.36	5.38	0.4
	0.5	5.07	5.30	4.77	5.05	4.80	4.12	4.47	4.41	5.45	4.90	3.58	0.5
	0.6	4.62	4.95	4.93	4.26	3.99	3.61	4.59	3.91	2.68	2.00	0.72	0.6
	0.7	6.95	5.83	5.25	5.23	4.49	4.67	2.44	0.94	0.73	0.30	0.06	0.7
	0.8	6.85	6.00	5.48	4.84	4.78	3.00	1.05	0.30	0.11	0.14	0.89	0.8
	0.9	7.94	6.89	5.16	7.14	3.88	3.01	0.67	0.18	0.31	2.35	1.32	0.9
1.0	7.92	7.03	7.92	8.35	4.98	2.30	0.59	0.65	1.42	2.37	1.54	1.0	
SnTe	SnSe	0.0	0.1	0.2	0.3	0.4	0.5	0.6	0.7	0.8	0.9	1.0	SnSe

Figure S12: Quality factor  $\beta$  heat map with associated raw data. Data in table is dimensionless, but has been scaled by a factor of 100 for convenience. The quality factor  $\beta$  is a carrier concentration independent proxy for  $zT$  which convolutes the intrinsic electronic and thermal transport. We can see that the simultaneous optimization of the intrinsic mobility and lattice thermal conductivity indicates a local maxima at an intermediate alloy – which does not lie upon any of the chemically intuitive lines studied by the literature.